RSC Advances

PAPER

View Article Online
View Journal | View Issue

Cite this: *RSC Adv.*, 2025, **15**, 36473

Fe/Ti decorated arsenene for phenoxyethanol detection: DFT and COHP analysis

Nawal Madkhali,[a] Muhammad Mushtaq, *[b] Turki Altoub,[a] Norah Algethami,[c] Amel Laref,[d] Amneh Shtaiwi,[e] Hamzah A. Qattous[f] and Yazen M. Alawaideh[g]

In the modern industrial era, the extensive release of toxic substances into the environment continuously poses a threat to human health. To minimize the loss, it is crucial to carefully monitor and detect such substances by developing efficient sensing materials. Adsorption of hazardous phenoxyethanol PE ($C_8H_{10}O_2$) was investigated on pristine and X = Fe/Ti modified arsenene using DFT and COHP calculations. The stability of the dopants (adsorbents) in/on arsenene was explored using the binding (adsorption) energy. In all four forms, the X-atom strongly binds to arsenene *via* p–d overlapping. The unpaired electrons of the X-atom induce magnetization in arsenene. Half-metallic or narrow band gap features can be obtained when arsenene is modified with an X-atom. The given molecule, due to the coulombic repulsion of the paired electrons on As atoms, is weakly adsorbed. However, adsorption is slightly enhanced for the Fe-decorated system and significantly improved for the Ti-decorated ones. Among all cases, the lowest adsorption energy of −2.5 eV was obtained for Ti-adsorbed arsenene ($As_{50}Ti$) due to reasonable charge exchange, change in actual charge density, and work function. The molecule interacts chemically with $As_{50}Ti$ by forming a Ti–C bridge. The DOS and COHP analysis show that this interaction originates from the overlapping of the Ti-3d orbital with the C-2p of the molecule. The ICOBI analysis predicts a mixed covalent-ionic bonding for the Ti–C pair. The Gibbs free energy calculations reveal that the adsorption of PE has a spontaneous behavior at room temperature. This atomic-level study offers a profound understanding of the interaction between PE and arsenene systems, which is beneficial in designing the desired sensing materials.

Received 17th August 2025
Accepted 24th September 2025

DOI: 10.1039/d5ra06078h

rsc.li/rsc-advances

1. Introduction

Volatile organic compounds (VOCs) are a large group of organic compounds we regularly encounter in household items like paints, furniture, cleaning supplies, and cosmetics, which release gases we breathe in. Many VOCs may harm health, causing cancer, respiratory issues, and discomfort. Despite this, community awareness of VOCs and their risks is low. Detecting VOCs *via* sensors is crucial for reducing hazardous effects and ensuring a safe environment.[1]

Two-dimensional (2D) materials possess exceptional electrical, mechanical, and chemical properties, suitable for applications in electronics, catalysis, energy storage, and environmental sensing.[2,3] Following the discovery of graphene, numerous additional 2D materials like silicene, phosphorene, and arsenene have been realized.[4,5] A successful way to customize 2D materials' electrical and magnetic properties is surface modification *via* doping or decorating with transition metal (TM) atoms.[6] Titanium (Ti) has been interesting for doping due to its partially filled d-orbitals, which can boost surface reactivity and create localized magnetic moments.[7–9]

Limited understanding exists of how pristine and Ti-decorated arsenene differ in adsorption, magnetic behavior, and electronic structure, despite recent studies on their potential for gas sensing and energy storage. Graphene and similar layered materials are promising for gas sensing due to high surface activity and large surface area.[10] Furthermore, no comprehensive study has employed first-principles calculations to examine the adsorption of $C_8H_{10}O_2$ on 2D materials, which is significant for environmental monitoring and breath analysis.

Arsenene has gained attention for its semiconducting nature, structural anisotropy, and potential for tuning *via* strain or functionalization.[11,12] Monolayer arsenene has a tunable band gap, unlike its bulk form, indicating potential in optoelectronic and nanoelectronic devices.[13]

[a]*Department of Physics, College of Sciences, Imam Mohammad Ibn Saud Islamic University (IMSIU), Riyadh 13318, Saudi Arabia*

[b]*Department of Physics, University of Poonch Rawalakot, Rawalakot 12350, AJK, Pakistan. E-mail: mushtaq325@gmail.com*

[c]*Department of Physics, College of Science, Taif University, Taif 21944, Saudi Arabia*

[d]*Physics Department, College of Science, King Saud University, Riyadh, Riyadh Province, 11451, Saudi Arabia*

[e]*Chemistry Department, Faculty of Science, Applied Science Private University, Amman, 11931, Jordan*

[f]*Department of Basic Sciences, Middle East University, Amman 11831, Jordan*

[g]*MEU Research Unit, Middle East University, Amman 11831, Jordan*

Our literature survey reveals that the adsorption of phenoxyethanol on arsenene has not yet been studied experimentally or theoretically. However, the interaction of various VOCs and other substances on arsenene has been thoroughly explored in DFT simulations.[14–18] Recently, using DFT calculations, we investigated how Mn and Cr atoms facilitate chemisorption for pentanal on arsenene.[14] In another study, we explored the effect of aluminum (Al) and tin (Sn) decoration on the adsorption of hexanal on arsenene. It was found that in the presence of Al, arsenene showed a strong chemisorption for the hexanal and its electronic structure is extensively modified due to the overlap of interacting orbitals.[15] *m*-Xylene and toluene exhibit physisorption on square-octagon arsenene.[17] Similarly, hexane and heptane also show physisorption on delta-arsenene nanoribbon.[18] These studies demonstrate the potential of arsenene for the detection of VOCs. However, the weak chemical reactivity and selectivity of arsenene, which are common in pure 2D materials, restrict its practical applications, especially in gas sensing and catalysis.[19]

Recent developments in computational materials science have enabled the use of first-principles techniques based on density functional theory (DFT) to study the behavior of low-dimensional systems accurately.[20] By using these methods, scientists can explore atomic-level interactions that are otherwise hard to observe experimentally, such as spin polarization effects, orbital hybridization, and charge redistribution. DFT-based simulations are now an essential tool for predicting how 2D materials will behave under different modifications, which accelerates the process of discovering and optimizing materials for specific applications.[21–23] In addition, DFT can accurately predict the properties of materials under various conditions.[24–26]

Phenoxyethanol (PE), with a chemical composition of $C_8H_{10}O_2$, is a colourless liquid with a rose-like odour, belongs to glycol ethers, and is used in perfumes, insect repellents, and other applications. This organic compound can be synthesized *via* various routes.[27–29] PE demonstrates antimicrobial properties, serving as an effective preservative in pharmaceuticals, cosmetics, and lubricants. The main hazards of PE relate to its toxicologic properties. It is toxic through inhalation, ingestion, and skin contact. Exposure may occur when used as a cosmetic, perfume, or soap fixative. Although often considered safe at low dose concentrations, it may induce skin and eye irritation as well as allergic reactions in specific individuals.

This study investigates how X-atom (X = Fe or Ti) modifies the adsorption capability of arsenene toward PE. It provides an opportunity to design arsenene for catalysis and gas sensing applications. We evaluated the sensing capability by analyzing adsorption energy, electronic properties, chemical bonding and charge transfer. The purpose of this research is to provide a fundamental understanding of designing functionalized arsenene for PE-based sensors.

2. Computational method and detail

This study involves the first-principles calculations based on density functional theory (DFT). All the calculations are performed using the Vienna *Ab initio* Simulation Package (VASP).[22,23,30] Fundamentally, the code solves the total energy equations using plane waves and a pseudopotential approach. The plane-waves were expanded using a kinetic energy cut-off of 500 eV. The electron–ion interactions were treated using the projector-augmented wave method. The unknown exchange–correlation energy was approximated in the generalized gradient approximation (GGA) of Perdew–Burke–Ernzerhof (PBE).[31] To obtain the ground structure and its electron density, a complete scheme of relaxation, including the volume and shape of the cell and atomic positions, is used in the conjugate gradient (CG) algorithm. The ions were allowed to move to minimize the net forces below -0.01 eV Å^{-1}. The energy criterion of 1×10^{-4} eV was applied during the electronic iterations. As is known the normal DFT does not properly handle the effects of strongly correlated d-orbital electrons, we have externally added some amount of onsite Coulomb interaction U and exchange interaction energy J in the calculations. Such modified DFT method is commonly known as DFT+U_{eff}, where $U_{\text{eff}} = U - J$. In our calculations, we have used DFT+U_{eff} by taking the U_{eff} value of 3.29 and 2.58 eV, respectively, for the Fe and Ti atom.[32] Periodic boundary conditions were imposed in the z-direction normal to the surface of the arsenene, such that periodic images have a separation of 30 Å. Weak van der Waals interactions were treated in DFT+D3 approach.[33] A $5 \times 5 \times 1$ supercell of perfect monolayer arsenene (p-As) in buckled phase (also known as β-As) was used as the basic structure model. For this supercell size, the Brillouin zone integration was performed using a $6 \times 6 \times 1$ grid, which was increased to $9 \times 9 \times 1$ for the density of states (DOS) calculations. The binding strength of the dopants with arsenene is calculated as.[34]

$$E_b = (E_{\text{SV-As}} + E_X) - E_{\text{X-As}} \quad (1)$$

where $E_{\text{SV-As}}$, E_X, and $E_{\text{X-As}}$ represent the ground state DFT energy of arsenene with a single vacancy (SV-As), isolated X atom, and X-doped arsenene (X-As), respectively.

To estimate the adsorption stability of the adsorbed atoms and PE, the adsorption energy (E_{ads}) was calculated using eqn (2).[35]

$$E_{\text{ads}} = E_{AB} - (E_A + E_B) \quad (2)$$

where all terms on the right side correspond to the ground state energy, AB is the product, A and B are the reactants. E_B is taken from the DFT energy of the isolated atom or molecule.

The chemical bonding analysis was performed with the LOBSTER code.[36] The geometries and electron localized function (ELF) plots were plotted using the VESTA code.[37] We acknowledge Professor Wang and his team for developing the VASPKIT tool.[38]

3. Results and discussion

3.1 Pristine arsenene

Arsenene, the monolayer (ML) of arsenic (As) atoms, is obtained from the bulk arsenic. Bulk arsenic has a layered structure,

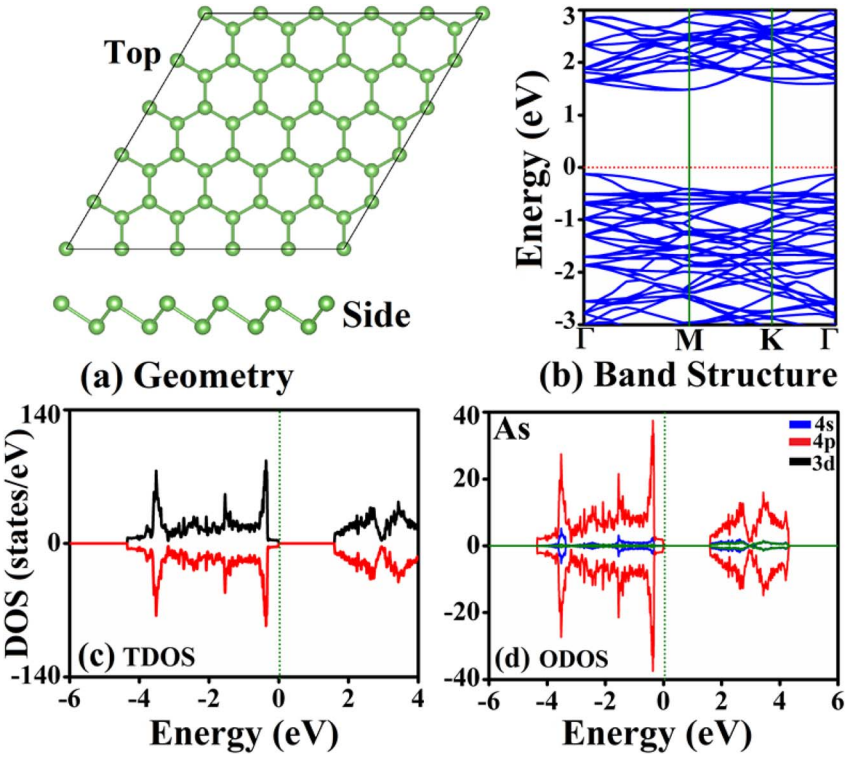

Fig. 1 Pristine arsenene; (a) relax geometry, (b) band structure, (c) total density of states (TDOS), (d) orbital DOS (ODOS). The Fermi level (E_F) is set at 0 eV.

where weak interactions separate atomic layers. Top and side views of the ground state geometry of pristine arsenene (ML-As) are shown in Fig. 1(a). The material has a hexagonal lattice of As atoms arranged in a honeycomb pattern with some buckling in the out-of-plane direction, as shown in the side view. This system has a buckled structure composed of two atomic planes of As-atoms separated by a specific distance called the buckling height. The top view shows that the material has a graphene-like honeycomb structure where each As-atom is bonded to three neighboring As-atoms. The calculated in-plane lattice constant is 3.60 Å, the bond length of two connected As-atoms is 2.50 Å and the bond angle at each As-atom is 95°. In Fig. 1(b), the electronic band structure of p-As is displayed along high-symmetry sites in the Brillouin zone (Γ, M, K, and T). In the zero-electron volt region, the Fermi energy lies within the band gap, confirming the absence of charge carriers. The figure emphasizes the conduction and valence bands, which represent the semiconducting behavior with an indirect PBE band gap of 1.59 eV, following the literature.[5] Such fundamental properties of p-As and its derivatives are shown in Table S1 of the SI. In general, the density of states (DOS) of a system in DFT theory describes the proportion of states that are to be occupied by the system at each energy. The results show that 4s-orbitals dominate the deep orbitals, with no 3d-orbital occupied, implying no magnetic properties. The orbital resolved DOS (Fig. 1(d)) reveals that among the three orbitals, the 4p-orbital has a dominant contribution to electronic states across the Fermi level. It confirms that the electronic properties of arsenene are strongly controlled by the 4p electrons.

3.2 Chemically modified arsenene

To tune the basic and sensing properties, arsenene is modified chemically by doping or surface decoration with X-atom (X = Fe, Ti). Four new systems are obtained, two doped and two decorated; (i) Fe-doped arsenene, where an Fe atom replaces one As atom, (ii) Ti-doped arsenene, where one Ti atom replaces one As atom, (iii) Fe-decorated arsenene, where one Fe atom is adsorbed on arsenene, (iv) Ti-decorated arsenene, where one Ti atom is adsorbed on arsenene.

3.3 Fe-doped arsenene ($As_{49}Fe$)

The initial geometry of Fe-doped arsenene, named $As_{49}Fe$, is shown in Fig. 2(a). The actual lattice before doping is composed of fifty As atoms (As_{50}), and after the doping of one Fe atom, it becomes $As_{49}Fe$. Due to different attributes of Fe, the doped atom may experience imbalanced forces from the neighboring As atoms. This effect may allow the doped atom to displace from the actual site to occupy a site with minimum forces. The final geometry of $As_{49}Fe$ is shown in Fig. 2(b). The insertion of the Fe atom causes modifications in bond lengths and angles in the structure. The calculated As–Fe bond length is 2.50 Å, slightly greater than the initial value of 2.47 Å. The As–Fe–As bond angle is 105°, greater than the initial value of 92°. The change in bond length and bond angle at the doping site indicates local deformation of the original symmetry of the arsenene. The obtained binding energy of the Fe-atom in arsenene 4.76 eV per atom, supports the literature.[34] The binding energy defined in eqn (1) indicates that doping is favorable. These deformations may

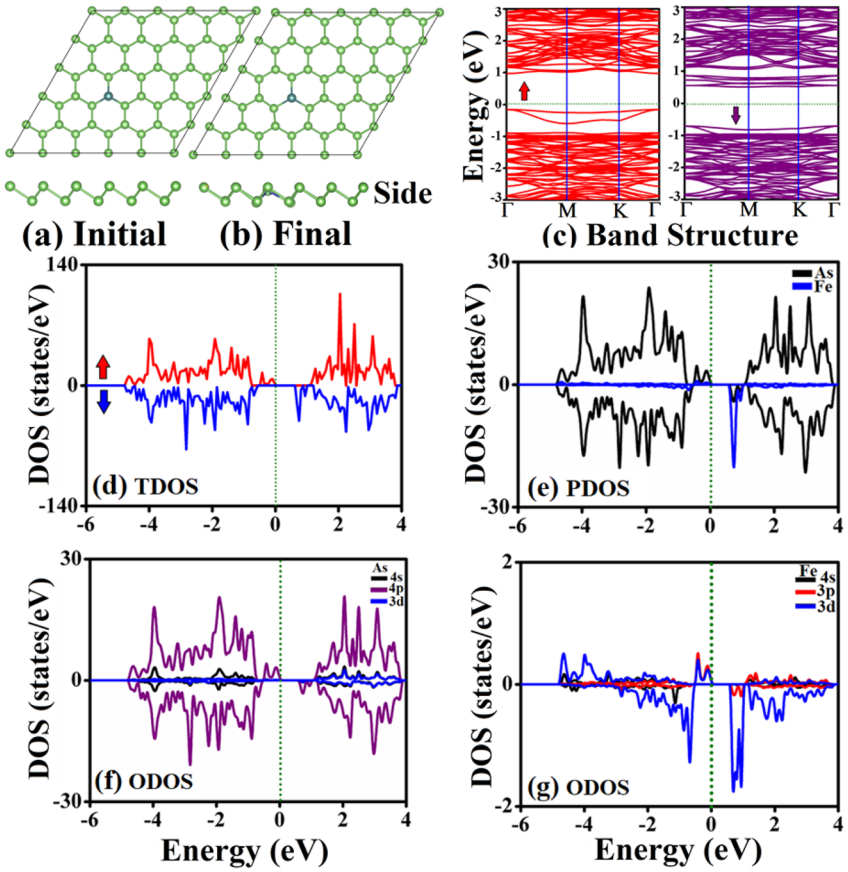

Fig. 2 Single Fe-atom doped arsenene ($As_{49}Fe$); (a) initial structure, (b) final structure, (c) band structure, (d) TDOS, (e) PDOS of As and Fe-atom, (f) ODOS of As-atom, (g) ODOS of Fe-atom.

impart interesting new features to arsenene, which will be discussed in the following sections.

The total energy calculations revealed that $As_{49}Fe$ is magnetic in the ground state. The induced magnetism is mainly attributed to the Fe atoms. The system's total magnetic moment (M) is $4.2\mu_B$. The Fe atom carries a moment of $3.6\mu_B$, and each As atom connected to the Fe atom has a moment of $0.2\mu_B$. The positive sign of the moment of the As atoms indicates ferromagnetic coupling between the Fe atom and the As atoms.

The electronic band structure of $As_{49}Fe$ in Fig. 2(c) and total DOS in Fig. 2(d) shows the half-metallic character of the material. It is caused by the contribution of iron (Fe) to the 3d orbital, which has strong spin-polarized properties. The material is metallic for the majority spin electrons and a semiconductor for the minority spin electrons. Such a high difference between the electronic states for two types of electrons at the Fermi level creates high spin polarization, which causes magnetism. The PDOS in Fig. 2(e) indicates that band edges are dominated by the As-atoms, and the ODOS plots in Fig. 2(f) and (g) show that the Fe-d orbital has large spin splitting, which is responsible for the observed significant magnetic moment of the Fe-atom. The Fe-3d and As-4p hybridization redistributes the electronic charge, which induces spin-polarization in the As-atom. This leads to the As atoms in the 4p orbital gaining weight near the Fermi level, whereas the 4s orbital remains essentially inert near the Fermi level.

3.4 Fe-adsorbed arsenene ($As_{50}Fe$)

To decorate the As with the Fe atom, the Fe atoms are initially placed at four high-symmetry sites above the surface of the As, shown in Fig. S1 of the SI. The combined system is $As_{50}Fe$. These highly symmetric sites include the top site (T-site), valley site (V-site), hollow site (H-site), and bridge site (B-site).

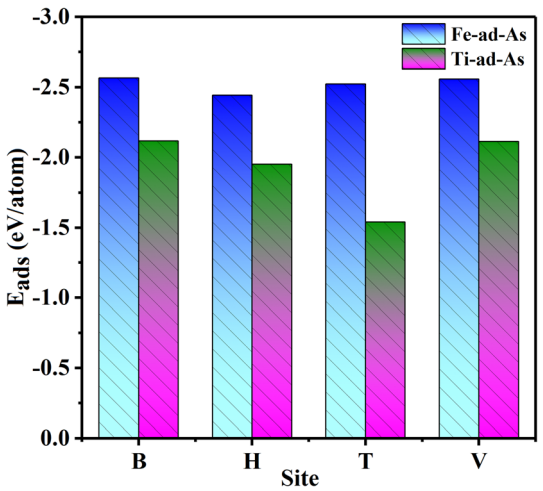

Fig. 3 Adsorption energy for single X-atom (X = Fe or Ti) adsorbed arsenene at bright (B), hollow (H), top (T), and valley (V) sites.

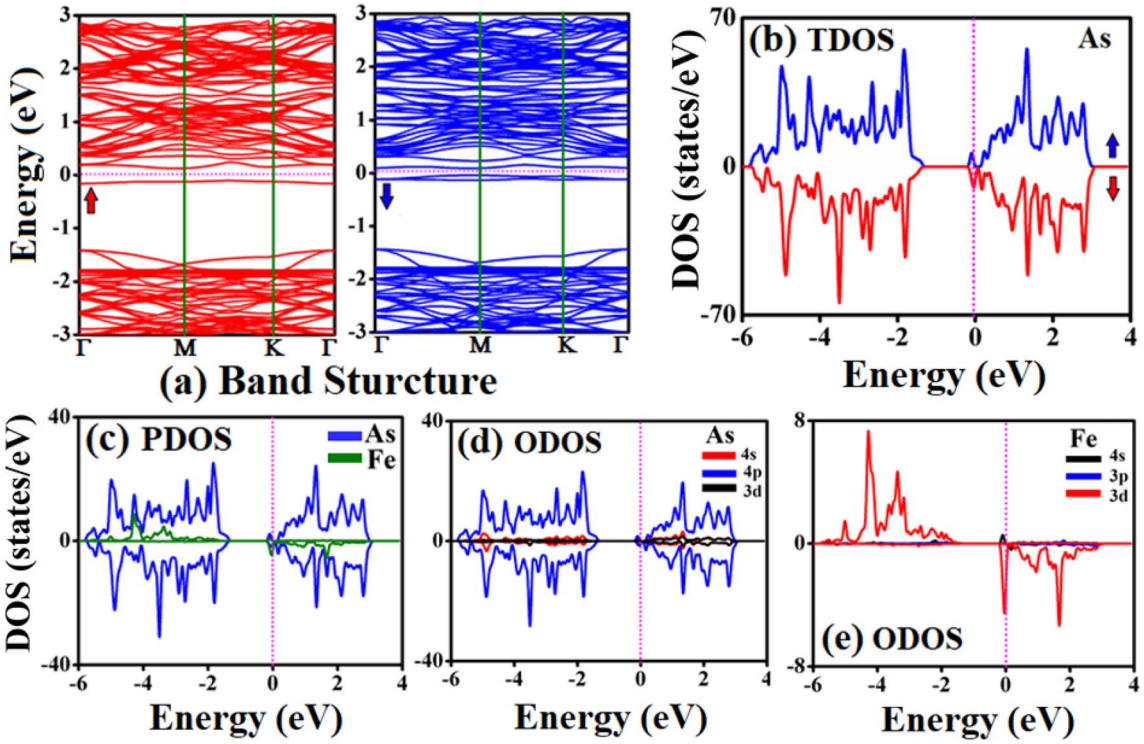

Fig. 4 Single Fe-atom adsorbed arsenene ($As_{50}Fe$); (a) band structure, (b) TDOS, (c) PDOS of As and Fe-atom, (d) ODOS of As-atom, (e) ODOS of Fe-atom.

Fig. S2 displays the relaxed geometries of these decoration configurations. The related calculated adsorption energy (E_{ads}) is shown in Fig. 3. It reveals that the H-site has the lowest adsorption energy. Therefore, this site is marked as the most favorable site. All the electronic and magnetic properties of $As_{50}Fe$ are hence calculated only for $As_{50}Fe$ in the H-site configuration. The As–Fe bond length is 2.50 Å, greater than the As–Fe bond length found in $As_{49}Fe$. The larger value of the bond length is due to the weak coupling between the Fe atom and its neighboring As atom. As a result, the $As_{50}Fe$ has a relatively larger value of M of 3.76μ_B, greater than the M value found in $As_{49}Fe$. The Fe and As atoms have a partial moment of 3.71 and 0.06μ_B, respectively.

The band structure of $As_{50}Fe$ in Fig. 4(a) and TDOS in Fig. 4(b) both confirm that $As_{50}Fe$ has a semiconducting character. The calculated band gap is 0.14 eV. The PDOS plot in Fig. 4(c) demonstrates that the As atom has a significant contribution to the valence band and conduction band states. In contrast, due to its small percentage, the Fe atom has a negligible contribution to the formation of band edges. The ODOS in Fig. 4(d) and (e) shows that As-4p states have a dominant contribution in the electronic states below and above the Fermi level. The ODOS of the Fe atom helps us in understanding the source of magnetism in $As_{50}Fe$. We noticed that the Fe-d orbital has an obvious antisymmetric distribution in two spins, which induces a net magnetic moment in the material.

3.5 Ti-doped arsenene ($As_{49}Ti$)

Similar to $As_{49}Fe$, the $As_{49}Ti$ is obtained by replacing one As atom in arsenene with one Ti atom. Initial and final geometry and electronic properties are displayed in Fig. 5. Our observations revealed a slight displacement of the doped Ti-atom from its initial position, resulting in a slight deformation and a shift of the hexagonal rings downward. The downward displacement was probably due to the push from the surrounding As-atoms. The computed binding energy is 5.62 eV per atom. The As–Ti bond is 2.57 Å, which is marginally longer than the original value of 2.50 Å. Compared to the initial value of 92°, the As–Ti–As bond angle is now 100°. By changing the link length and bond angle at the doping location, the original symmetry of the lattice has been locally distorted. These deformations may give arsenene some interesting properties. In the ground state, $As_{49}Ti$ is magnetic, according to the total energy calculations. In particular, the Ti atoms are responsible for the induced magnetism. The entire system has a moment of 1μ_B. The moment of the first neighboring As atoms is −0.037μ_B, while the moment of the Mn atom is 1.006μ_B. Antiferromagnetic coupling between the Ti and As atoms is indicated by the As atom moment's negative sign. Consequently, the overall magnetization is decreased. The electronic band structure and the total DOS both show that the material is half-metallic, such that the material is metallic for majority spin and semiconducting for the minority spin electrons. The electronic states of the two types of electrons differ significantly at the Fermi level, leading to strong magnetism and spin polarization. The As-atoms dominate the band edges, according to the PDOS, and the Ti-d orbital has significant spin splitting, which accounts for the Ti-atom's observed intense magnetic moment, according to the ODOS plots.

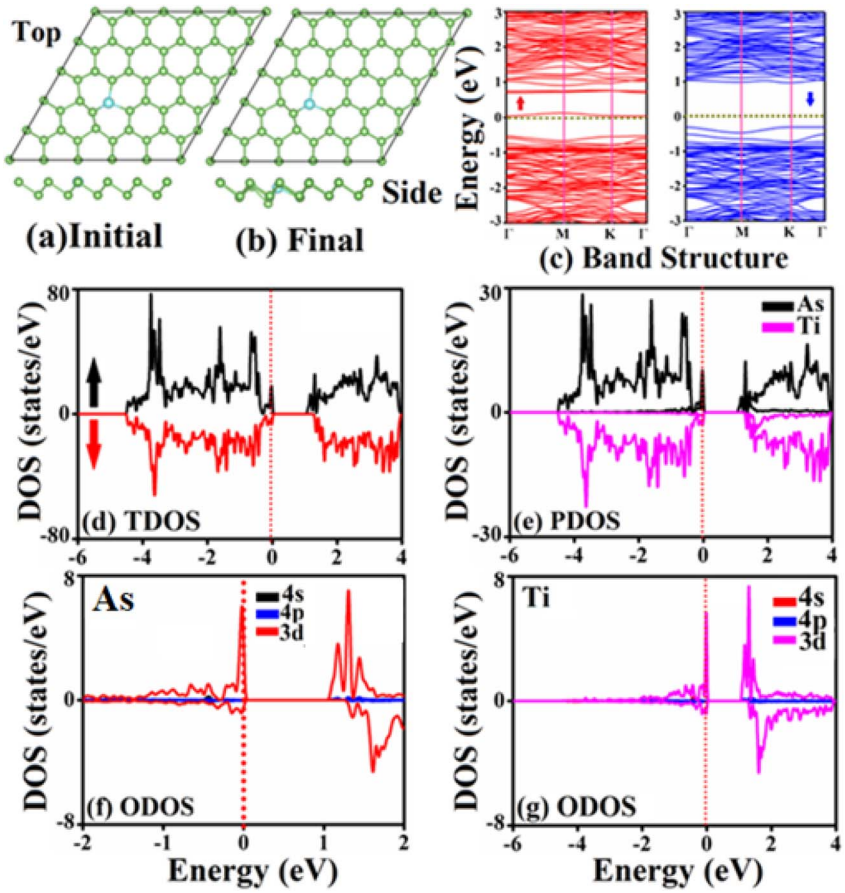

Fig. 5 $As_{49}Ti$; (a) initial structure, (b) final structure, (c) band structure, (d) TDOS, (e) PDOS of As and Ti-atom, (f) ODOS of As-atom, (g) ODOS of Ti-atom.

3.6 Ti-adsorbed arsenene ($As_{50}Ti$)

In arsenene decorating with Ti ($As_{50}Ti$), the Ti atom is initially placed at four symmetry sites, as mentioned in Fig. S1. Thus, a total of four adsorption configurations are obtained. To achieve the lowest energy adsorption configuration, each configuration was fully relaxed, and its adsorption energy was calculated, as shown in Fig. 3. The H-site configuration yields the lowest E_{ads}. As a result, only this configuration is considered for further analysis. The As–Ti bond length of 2.71 Å is longer than the As–Ti bond length of 2.71 Å in the doping case. The As–Ti–As bond angle is 81°. For $As_{50}Ti$, the value of M is $2.3\mu_B$, where Ti atom has a moment of $1.7\mu_B$ and each connected As atom has a small moment of $+0.2\mu_B$. The band structure and TDOS confirm the semiconducting nature of $As_{50}Ti$ in Fig. 6(a) and (b) with a band gap of 0.13 eV. According to PDOS in Fig. 6, the As atom plays a significant role in the valence band and conduction band states. In contrast, the tiny percentage of Ti atoms means that they make a minimal contribution to the formation of band edges. The ODOS demonstrates that As-4p states dominate the electronic states below and above the Fermi level.

3.7 Phenoxyethanol ($C_8H_{10}O_2$) on pristine arsenene

Detecting and monitoring the concentration of PE requires sensitive detection materials to be used in sensor manufacturing. Computationally, the ability of a material to detect a given substance is determined by the adsorption energy and related parameters. These parameters themselves may depend on various other factors such as the nature of the environment, the orientation of the landing substrate, and its position on the surface of the detecting material. To accurately predict the adsorption energy and its strength, various initial orientations (IO) of the PE relative to the adsorbent's surface, and various adsorption sites (AS) are considered. The product of IO and AS yields the number of adsorption configurations (ACs). The number of AS depends on the chemical composition and atomic structure of the substance. In p-As, there are four distinct AS covering top (T), hollow (H), bridge (B), and valley (V), all of which are well described in the literature. For a large-sized molecule, the two main IOs are horizontal and vertical relative to the adsorbent, while the IO. For all AC, the adsorption energy is calculated. Among all, the lowest energy is considered for further analysis of the properties. In case of PE on p-As, three different horizontal (h1, h2, h3) and two vertical (v1, v2) orientations were involved. The calculated adsorption energy is −0.49, −0.41, −0.43, −0.2, and −0.15 eV, respectively, for h1, h2, h3, v1, and v2 orientations. All these values are minimal, and the molecule moves away from the adsorbent in the final configuration. It shows that arsenene cannot capture

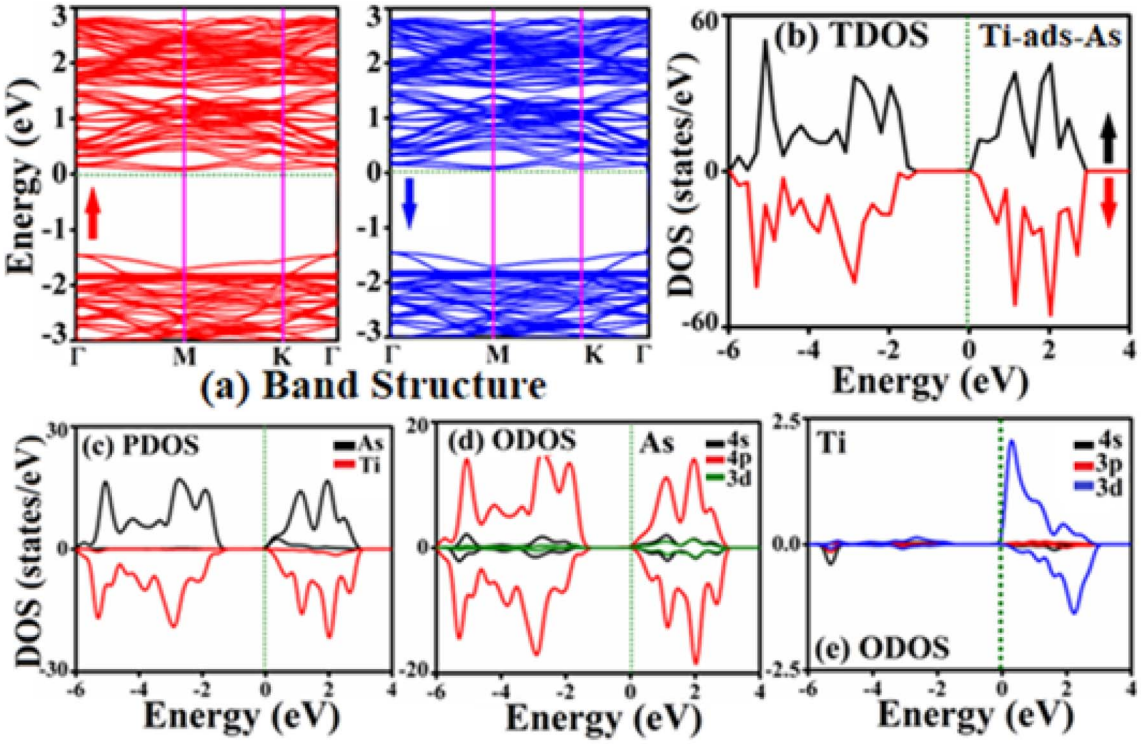

Fig. 6 $As_{50}Ti$; (a) band structure, (b) TDOS, (c) PDOS of As and Ti-atom, (d) ODOS of As-atom, (e) ODOS of Ti-atom.

the molecule and the resulting adsorption is weak, termed as physisorption. Therefore, the molecule with arsenene (p-As/PE) will not be discussed in detail.

3.8 Phenoxyethanol ($C_8H_{10}O_2$) on Fe/Ti modified arsenene

The central theme for introducing Fe/Ti atoms in arsenene is to tune the adsorption strength for PE molecule and achieve a strong detection. The initial ACs for the X (X = Fe or Ti) doped arsenene are shown in Fig. S4, and for the X adsorbed arsenene systems in Fig. S5. A comparison of the adsorption energy of some other VOCs is documented in Table S2. Each configuration is relaxed in the ground state, and its adsorption energy and adsorption height h are calculated, shown in Fig. 7 and Table 1. In this figure, the adsorption energy is taken in absolute form ($|E_{ads}|$). We find that the lowest E_{ads} (the highest $|E_{ads}|$) is achieved when PE is adsorbed on $As_{50}Ti$. Therefore, for further discussion, we consider only this case. The geometries of final ACs for PE on $As_{50}Ti$ ($As_{50}Ti$/PE) are shown in the main manuscript in Fig. 8. Accordingly, the final configurations for the PE on $As_{49}Fe$, $As_{50}Fe$, and $As_{49}Ti$ are shown in Fig. S6, S7, and S8, respectively. According to Fig. 8, in all ACs, the molecule interacts with the adsorbent ($As_{50}Ti$) through the Ti atom. In h-C, the adsorbent ($As_{50}Ti$) is through the Ti atom. In h-C and h-H configuration, the C-atoms of the molecule interact with the Ti-atom, forming a Ti–C bridge. For the h-O case, the C and O-atoms interact with the Ti-atom, leading to two types of bridges, Ti–C and Ti–O. In v-H, the interaction is through Ti–H, and in v-O, the Ti–O bridge facilitates the interaction. The E_{ads} −2.56, −2.58, −1.48, −0.21, −1. The E_{ads} value is −2.56, −2.58,

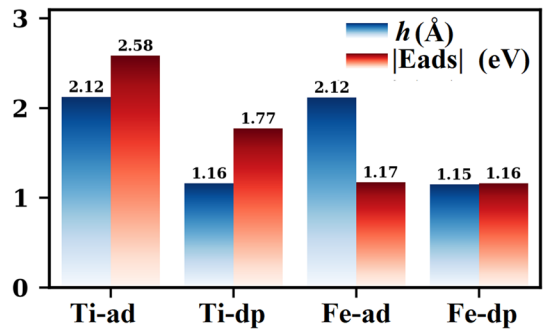

Fig. 7 Final adsorption height (h) and absolute adsorption energy $|E_{ads}|$ for $C_8H_{10}O_2$ on doped and decorated arsenene systems.

Table 1 Adsorption energy E_{ads} for $C_8H_{10}O_2$ on pristine arsenene (p-As: As_{50}), single X atom (X = Fe or Ti) doped arsenene ($As_{49}X$), and single X-atom adsorbed arsenene ($As_{50}X$) in various horizontal (h-C, h-H, h-O) and vertical (v-H, v-O) orientations. The lowest energy configuration for each adsorbent is marked in bold

	E_{ads} (eV per molecule)				
Orientation	p-As	$As_{49}Fe$	$As_{50}Fe$	$As_{49}Ti$	$As_{50}Ti$
h-C	**−0.49**	−0.96	−1.03	−1.24	−2.56
h-H	−0.41	−1.05	**−1.17**	−1.51	**−2.58**
h-O	−0.43	**−1.17**	−0.93	**−1.77**	−1.46
v-H	−0.21	−0.53	−0.36	−0.95	−0.21
v-O	−0.16	−1.14	−0.92	−1.61	−1.41

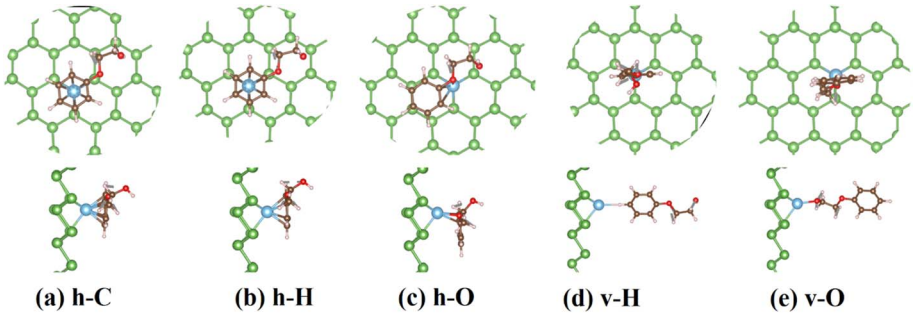

Fig. 8 Final adsorption configurations of molecule on single Ti-atom adsorbed arsenene ($As_{50}Ti$) in orientation; (a) h-C, (b) h-H, (c) h-O, (d) v-H, (e) v-O.

−1.46, −0.21, and −1.4 eV, respectively, for h-C, h-H, h-O, v-H, and v-O orientation. Thus, the v-H case has the lowest E_{ads}. In the following sections, we will consider only this case for the analysis of the electronic properties of PE on $As_{50}Ti$.

3.9 Electronic properties of $As_{50}Ti$/PE

The observed chemisorption of PE on $As_{50}Ti$ may alter the actual electronic properties of these two reactants. To examine how these properties evolve after adsorption, the band structure and DOS plots are calculated and displayed in Fig. 9. In the projected band structure in Fig. 9(a), the contribution of As, Ti, and molecule is shown in red, blue, and green. We find that the Ti and molecule mainly contribute to the valence band top. The conduction band bottom has a substantial contribution from the As atoms. To under how new states emerge near the Fermi level, DOS plots are involved. TDOS shows that the maximum states in the valence band belong to the adsorbent; however, there is a considerable part of the states that originate from the

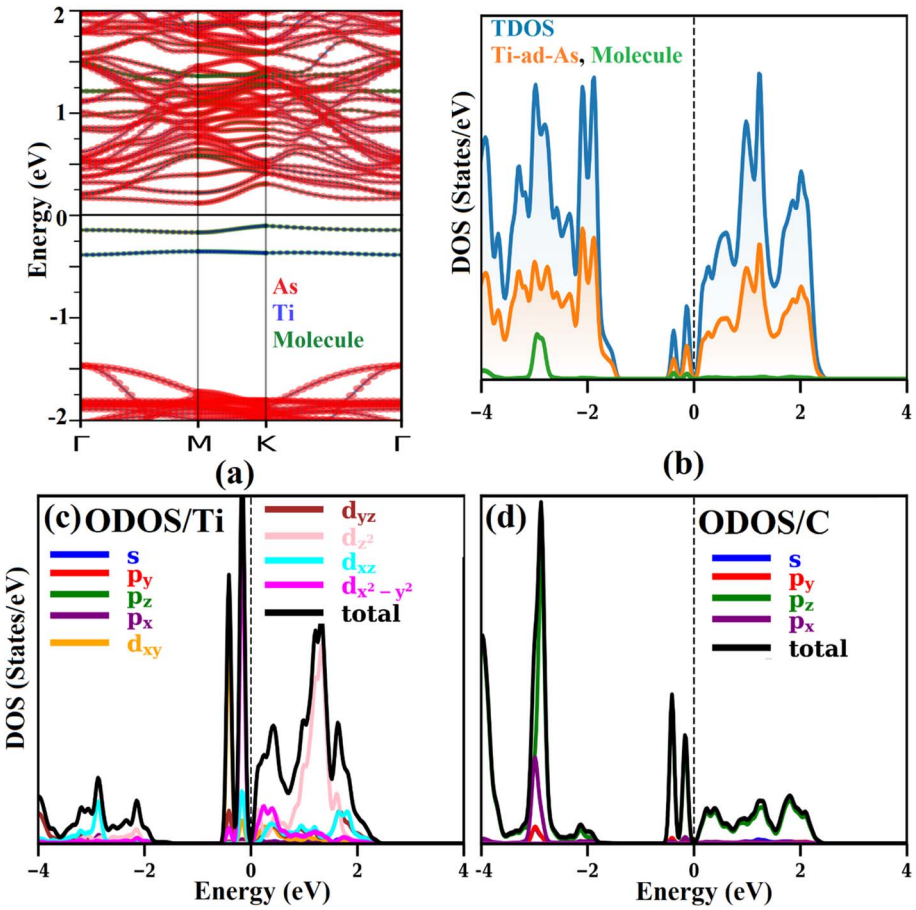

Fig. 9 $As_{50}Ti$ with molecule in the lowest energy configuration; (a) band structure, (b) total density of states, (c) orbital density of states (ODOS) for Ti-atom, and (d) ODOS for C-atom.

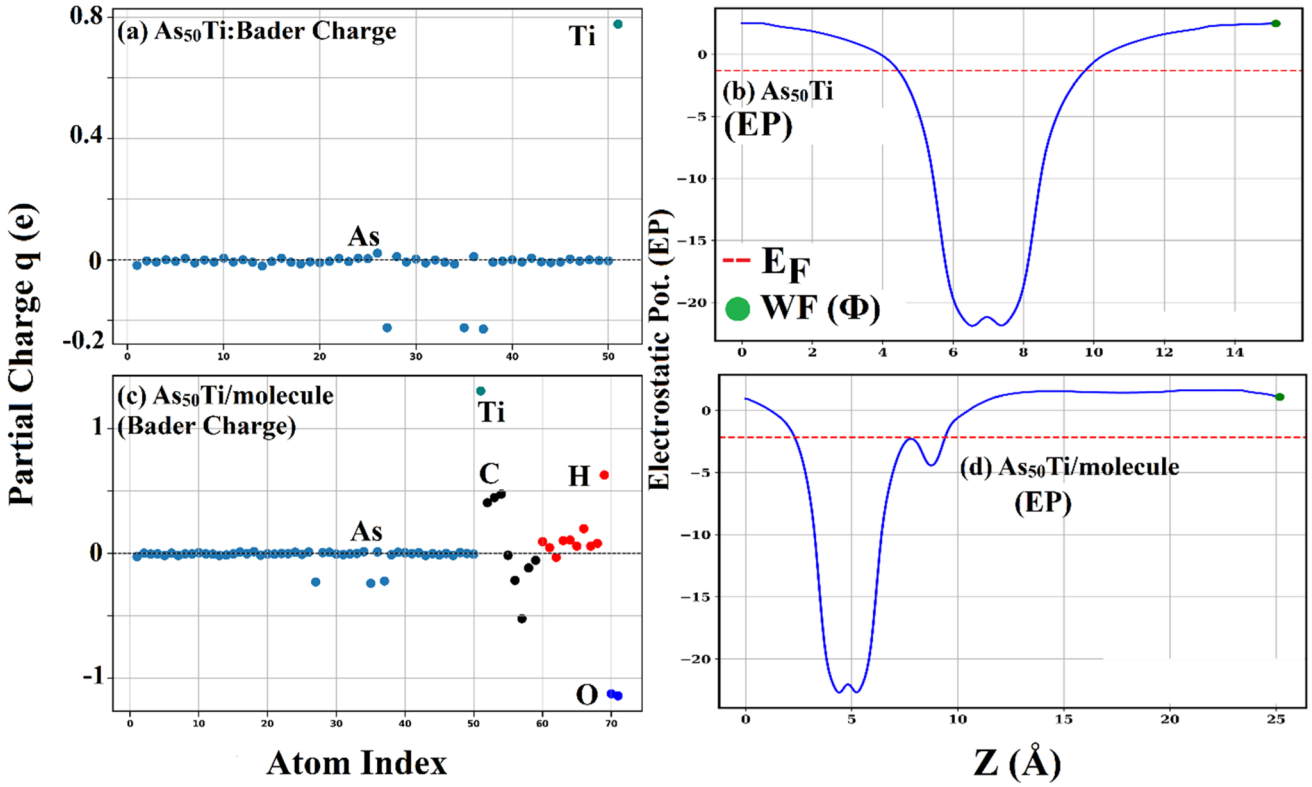

Fig. 10 Partial charge q and electrostatic potential EP for $As_{50}Ti$ and $As_{50}Ti$ with molecule ($As_{50}Ti$/molecule); (a) q for $As_{50}Ti$, (b) EP for $As_{50}Ti$, (c) q for $As_{50}Ti$/molecule, (d) EP for $As_{50}Ti$/molecule.

molecule. Similar to band structure, a narrow band gap is observed at the Fermi level in DOS plots. The ODOS for Ti and C atoms reveal that the interaction between PE and adsorbent originates from the overlapping of Ti-3d and C-2p orbitals. This p–d overlapping establishes a reasonably attractive binding between Ti and C, which stabilizes chemisorption. In addition, such orbital overlapping plays a key role in the exchange of charge, the change of electronic charge density, and the work function of the host material. Interestingly, the $As_{50}Ti$ system becomes non-magnetic after the adsorption of the molecule. This is because the unpaired electrons of the Ti atom are utilized in bonding with the C atoms of the molecule. To analyze the charge exchange, Bader charge analysis is performed, and its results are shown in Fig. 10. In this figure, the atom index indicates the position of each atom in the POSCAR file. For example, atom index 50 indicates the 50th atom in the POSCAR file. The reference line along the y-axis shows no charge exchange. The positive values of partial charge on each atom show charge donor character, while the negative value of q shows charge acceptor property. In Fig. 10(a), the partial charge is displayed for $As_{50}Ti$ without a molecule. It shows that some As atoms accept charge from the Ti atom. These As atoms are connected to the Ti atom. The Ti atom has a large net positive charge, showing its charge donation. The net partial charge on the Ti atom is $+0.8e$, and its nearest As atoms have a net partial charge of $-0.18e$. All other As atoms have a zero partial charge. When the molecule is adsorbed (Fig. 10(c)), charge exchange occurs between Ti atom and the nearest atom of the molecule. A close observation reveals that the partial charge on the As atoms does not change; however, the Ti atom loses more electrons while interacting with the molecule and bears a large net partial charge of $+1.4e$. Among the C, H, and O atoms of the molecule, some C atoms have a positive charge while some others have a negative charge. The C atoms with a negative charge are, in

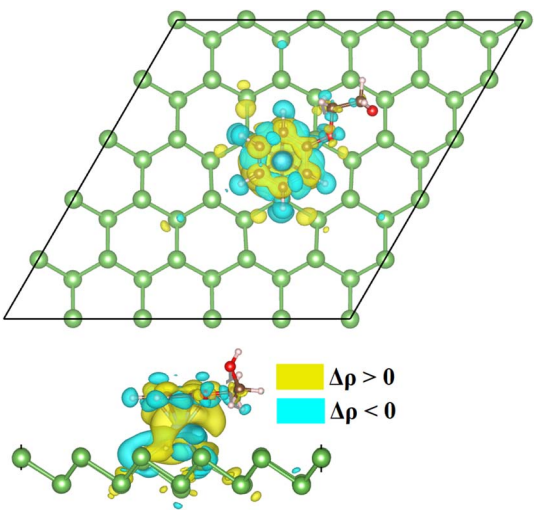

Fig. 11 Charge density difference (CDD) plot for $C_8H_{10}O_2$ on $As_{50}Ti$ in h-H orientation.

fact, in contact with the Ti atom, whereas the C atoms with a positive charge are far away from the Ti atom. Another interesting feature is that more than one C atoms have a negative charge. It confirms that the molecule interacts with the adsorbent's Ti atom through more than one C atom. Here, it is essential to mention that exchange of charge deforms the actual charge distribution, which leads to a change in the Fermi level position, and a shift in electron transport properties. One crucial parameter is the work function, which measures the energy required for electrons to be ejected from the material's surface. To better understand the change in work function, we have shown the electrostatic potential curves in Fig. 10(b) (without molecule) and Fig. 10(d) (with molecule). In the absence of a molecule, $As_{50}Ti$ has a Fermi energy and work function of −1.2 and 3.8 eV, respectively. When a molecule is adsorbed, it changes to −2.1 and 3.2 eV, respectively, for the Fermi energy and work function. The change in work function reflects the change in electrical conductivity of the material, which is used as a fingerprint for the detection of the molecule in the sensor. To further explore the interaction of molecules with adsorbents, charge density difference (CDD) is shown in Fig. 11. Here, charge exchange is shown in two distinct colors, yellow and cyan. The size of colored contours reflects the magnitude of change. Charge density is deformed at the interaction site on the adsorbent. The yellow region around the Ti atom shows charge transfer, and the cyan regions around the C atoms close to the Ti atom have charge accumulation. When interaction is strong, the charge density is more deformed, and more change occurs in the electronic and electrical properties of the adsorbent. All these changes provide helpful information in the sensing process.

To deeply understand how the molecule interacts with the adsorbent, crystal orbital Hamiltonian population (COHP) analysis is performed, shown in Fig. 12. In this analysis, the bonding and antibonding interactions are considered for the Ti–C pair. The bonding states induce stability in the bonding, whereas antibonding states cause instability. In the first plot, the bonding states are dominant far below the Fermi level, around −34 eV. The antibonding states also occur in the valence band around −16 and −8 eV below the Fermi level. These states weaken the binding strength between the C and Ti atoms. In addition, the small or no separation between bonding and antibonding states at the Fermi level also causes instability in the interaction. Further analysis of COHP for various orbital pairs shows that among Ti(3d)–C(2p), Ti(4p)–C(2p), Ti(4s)–C(2p), Ti(3d)–C(2s), Ti(4p)–C(2s), the deep bonding states around −34 eV belong to 4p–2s and 4p–2p orbital interactions. The states just below the Fermi level mainly belong to 3d–2p orbital interactions. As the states lie in the uppermost part of the valence band, they are energetically less stable. Such states occur when the chemical interaction between the two atoms is of moderate strength or weak. The ICOBI value for this Ti–C pair is found to be 0.50, which is an intermediate value between the two extreme values 0 and 1. Such a moderate value is an indication of a mixed covalent-ionic bonding between Ti–C pair. In short, the observed chemisorption for this molecule on $As_{50}Ti$ is

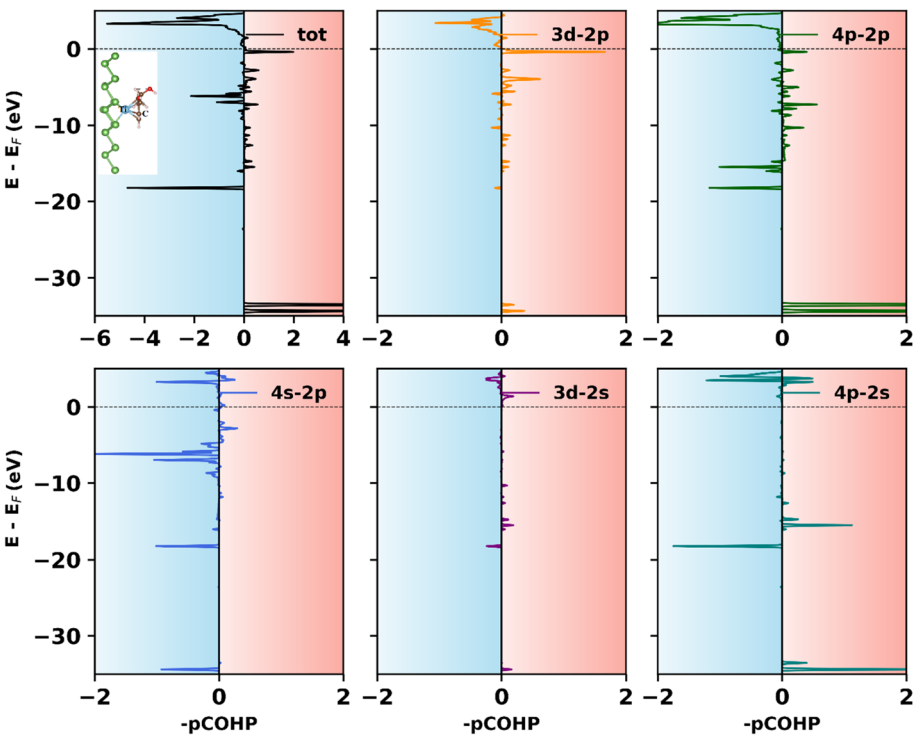

Fig. 12 Total and orbital-wise partial crystal orbital Hamiltonian population (−pCOHP) for Ti–C bonding pair in $As_{50}Ti$/molecule. Positive (negative) values of −pCOHP correspond to bonding (antibonding) states. The Fermi level is at 0 eV, marked in a dotted line. For better comparison, the *x*-axis scale is set the same for all orbital interactions.

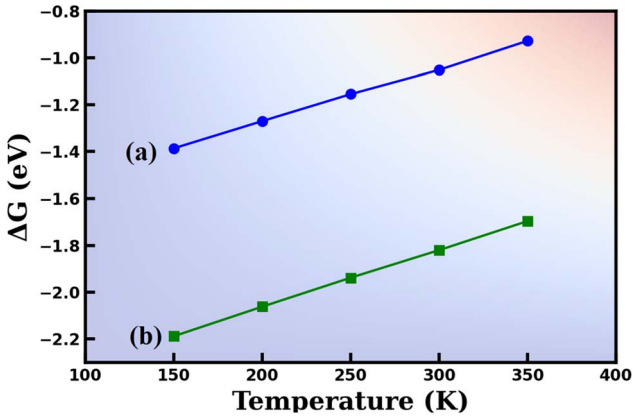

Fig. 13 Gibbs free energy (Δ*G*) for phenoxyethanol on (a) Ti-atom doped arsenene (Ti-dp-As), and (b) Ti-atom decorated arsenene (Ti-ad-As). The temperature *T* is varied in the range of 150–350 K. The pressure *P* is kept constant at 1 atm.

caused by the mixed covalent-ionic bonding, which occurs due to the overlapping of Ti-3d and C-2p orbitals.

3.10 Thermodynamics of adsorption

In the adsorption process, temperature plays a key role in the sensitivity of the sensing material. To address the effect, the thermodynamics of the adsorption are investigated by calculating the(Δ*G*) Gibbs free energy for adsorption (Δ*G*) at various temperatures (150–350 K) using the following expression (eqn (3)).[39]

$$\Delta G_{\text{ads}} = E_{\text{ads}} + \Delta E_{\text{ZPE}} - T\Delta S \quad (3)$$

where the 1st, 2nd, and 3rd term on the right side of eqn (1) represents the adsorption energy (at 0 K), zero-point energy (ZPE) correction and entropy contribution at temperature *T*. The results are shown below in Fig. 13.

It is clear that the adsorbed molecule shows spontaneous adsorption on both base materials, evidenced by the negative Gibbs free energy. However, the feasibility of the reaction decreases with temperature. In addition, the adsorption is more favorable for Ti-ad-As owing to its more negative Gibbs free energy. It can be assumed that at high elevated temperatures, the Gibbs free energy may become positive, where the adsorption would not be spontaneous. These results show that the adsorption of the given molecule is sensitive to temperature, but it can be predicted to be feasible at room temperature if other factors are ignored.

4. Conclusion

In this study, the adsorption of phenoxyethanol PE ($C_8H_{10}O_2$) was investigated on arsenene using first-principles based on density functional theory (DFT) calculations. Arsenene was modified using both doping and decoration of Fe and Ti atoms. Binding energy and adsorption energy confirm that the introduced defects are energetically favorable. These defects strongly influence the electronic and magnetic properties of the host material. The X and arsenic (As) atoms interact *via* ferromagnetic coupling. Half-metallic or narrow band gap features can be obtained when arsenene is modified with an X-atom. The given molecule shows physisorption on pristine arsenene. However, adsorption is slightly enhanced for Fe-decoration and strongly improved for Ti-decoration. Among all cases, the lowest adsorption energy of −2.5 eV was obtained for Ti-adsorbed arsenene ($As_{50}Ti$) due to reasonable charge exchange, change in actual charge density, and work function. The molecule interacts chemically with $As_{50}Ti$ by forming a Ti–C bridge. The DOS and COHP analysis show that this interaction originates from the overlapping of the Ti-3d orbital with the C-2p of the molecule. The ICOBI analysis predicts a mixed covalent-ionic bonding for the Ti–C pair. The thermodynamic analysis shows spontaneous adsorption for PE on the modified arsenene. This study promises Ti-element decorated arsenene as an effective sensing material for the development of PE-based sensors.

Conflicts of interest

There are no conflicts to declare.

Data availability

The data involved in this study will be made available upon request to the corresponding author.

Supplementary information is available. See DOI: **https://doi.org/10.1039/d5ra06078h**.

Acknowledgements

This work was supported and funded by the Deanship of Scientific Research at Imam Mohammad Ibn Saud Islamic University (IMSIU) (grant number IMSIU-DDRSP2503).

References

1 Y. Zhao, *et al.*, Fiber optic volatile organic compound gas sensors: A review, *Coord. Chem. Rev.*, 2023, **493**, 215297.
2 A. H. Khan, *et al.*, Two-Dimensional (2D) Nanomaterials towards Electrochemical Nanoarchitectonics in Energy-Related Applications, *Bull. Chem. Soc. Jpn.*, 2017, **90**(6), 627–648.
3 S. Raza, *et al.*, Electrochemistry of 2D-materials for the remediation of environmental pollutants and alternative energy storage/conversion materials and devices, a comprehensive review, *Sustainable Mater. Technol.*, 2024, **40**, e00963.
4 C. Kamal and M. Ezawa, Arsenene: Two-dimensional buckled and puckered honeycomb arsenic systems, *Phys. Rev. B: Condens. Matter Mater. Phys.*, 2015, **91**(8), 085423.
5 C. Kamal and M. Ezawa, Arsenene: Two-dimensional buckled and puckered honeycomb arsenic systems, *Phys. Rev. B: Condens. Matter Mater. Phys.*, 2015, **91**(8), 085423.

6 S. N. Reed-Lingenfelter, *et al.*, Surface Functionalization for Magnetic Property Tuning of Nonmagnetic 2D Materials, *Adv. Mater. Interfaces*, 2022, **9**(3), 2100463.
7 E. A. Humba, Computational Study of the Structure and Electronic Properties of Ag and Au Doped (TiO2)*n* Clusters (n = 2–6), MPhil thesis, University of Namibia, 2020.
8 C. X. Kronawitter, *et al.*, Titanium incorporation into hematite photoelectrodes: theoretical considerations and experimental observations, *Energy Environ. Sci.*, 2014, **7**(10), 3100–3121.
9 M. Fang and E.-H. Yang, Advances in two-dimensional magnetic semiconductors via substitutional doping of transition metal dichalcogenides, *Materials*, 2023, **16**(10), 3701.
10 S. Yang, C. Jiang and S.-h. Wei, Gas sensing in 2D materials, *Appl. Phys. Rev.*, 2017, **4**(2), 021304.
11 S. Sumanth Dongre, *et al.*, Review on 2D Arsenene and Antimonene: Emerging Materials for Energy, Electronic and Biological Applications, *Adv. Mater. Interfaces*, 2022, **9**(23), 2200442.
12 H.-S. Tsai, *et al.*, Direct Synthesis and Practical Bandgap Estimation of Multilayer Arsenene Nanoribbons, *Chem. Mater.*, 2016, **28**(2), 425–429.
13 X. Liang, *et al.*, Characterization of point defects in monolayer arsenene, *Appl. Surf. Sci.*, 2018, **443**, 74–82.
14 I. Muhammad, *et al.*, Enhanced Adsorption of Pentanal on M Atom (M = Mn, Cr)-Doped and Decorated Arsenene, *ACS Omega*, 2025, **10**(31), 34633–34644.
15 I. Muhammad, *et al.*, DFT study on Al/Sn-decorated arsenene: chemical bonding and adsorption of hexanal, *RSC Adv.*, 2025, **15**(12), 8938–8947.
16 V. Nagarajan, S. Sarvaka and R. Chandiramouli, Adsorption studies of nucleobases on ε-arsenene nanosheet based on first-principles research, *J. Mol. Graphics Modell.*, 2021, **103**, 107827.
17 M. S. Jyothi, V. Nagarajan and R. Chandiramouli, Square-octagon arsenene nanosheet as chemical nanosensor for M-xylene and toluene – A DFT outlook, *Comput. Theor. Chem.*, 2021, **1196**, 113088.
18 J. Princy Maria, V. Nagarajan and R. Chandiramouli, First-principles studies on sensing properties of delta arsenene nanoribbons towards hexane and heptane molecules, *Comput. Theor. Chem.*, 2021, **1201**, 113256.
19 Z. Xie, *et al.*, Chemistry, functionalization, and applications of recent monoelemental two-dimensional materials and their heterostructures, *Chem. Rev.*, 2021, **122**(1), 1127–1207.
20 W.-J. Yin, *et al.*, Recent advances in low-dimensional Janus materials: theoretical and simulation perspectives, *Mater. Adv.*, 2021, **2**(23), 7543–7558.
21 J. Hafner, Atomic-scale computational materials science, *Acta Mater.*, 2000, **48**(1), 71–92.
22 X. Ji, *et al.*, Floquet engineering of point-gapped topological superconductors, *Phys. Rev. B*, 2025, **111**(19), 195419.
23 N. Mardirossian and M. Head-Gordon, Thirty years of density functional theory in computational chemistry: an overview and extensive assessment of 200 density functionals, *Mol. Phys.*, 2017, **115**(19), 2315–2372.
24 Z. Ali, *et al.*, Advancements in Primary Radiation Damage Models and SRIM Simulations: A Review of Radiation Damage Predictions, *Nucl. Eng. Technol.*, 2025, 103570.
25 K. Rao, *et al.*, Comparable Study on Proton Radiation Effects for Amorphous and Crystalline $Ge_2Sb_2Te_5$, *IEEE Trans. Nucl. Sci.*, 2024, 1300–1308.
26 M. Haseeb, *et al.*, Doping effects in strontium hexaferrite: Theoretical and experimental analysis, *Mater. Today Commun.*, 2024, **41**, 110773.
27 B. Liu, *et al.*, Palladium-Catalyzed Bicycloaromatization of *o*-(Alkynyl)styrenes with Alkynes: Economical Access to Chrysene Derivatives, *Org. Lett.*, 2024, **26**(40), 8509–8514.
28 C. Liu, *et al.*, Rh(III)-Catalyzed C–H Annulation of *N*-Nitrosoanilines with Iodonium Ylides for the Synthesis of *N*-Alkyl Indoles, *J. Org. Chem.*, 2023, **88**(11), 7281–7289.
29 Z. Qi, *et al.*, Palladium-Catalyzed Aminosulfonylation of *ortho*-Iodoanilines with the Insertion of Sulfur Dioxide for the Synthesis of 3,4-Dihydro-benzothiadiazine 1,1-Dioxides, *Org. Lett.*, 2023, **25**(40), 7322–7326.
30 G. Kresse and J. Furthmüller, Efficient iterative schemes for ab initio total-energy calculations using a plane-wave basis set, *Phys. Rev. B: Condens. Matter Mater. Phys.*, 1996, **54**(16), 11169–11186.
31 J. P. Perdew, K. Burke and M. Ernzerhof, Generalized Gradient Approximation Made Simple, *Phys. Rev. Lett.*, 1996, **77**(18), 3865–3868.
32 C.-Y. Lin, *et al.*, Design Principles for Covalent Organic Frameworks as Efficient Electrocatalysts in Clean Energy Conversion and Green Oxidizer Production, *Adv. Mater.*, 2017, **29**(17), 1606635.
33 S. Grimme, *et al.*, A consistent and accurate ab initio parametrization of density functional dispersion correction (DFT-D) for the 94 elements H-Pu, *J. Chem. Phys.*, 2010, **132**(15), 154104.
34 M. Luo, Y. H. Shen and T. L. Yin, Structural, electronic, and magnetic properties in transition-metal-doped arsenene: Ab initio study, *Jpn. J. Appl. Phys.*, 2017, **56**(1), 015201.
35 I. Muhammad, *et al.*, Enhanced Sensing of S-VOCs on M-decorated (M = Li, Mg) Antimonene: DFT Insights, *J. Inorg. Organomet. Polym. Mater.*, 2025, DOI: **10.1007/s10904-025-03889-z**.
36 R. Nelson, *et al.*, LOBSTER: Local orbital projections, atomic charges, and chemical-bonding analysis from projector-augmented-wave-based density-functional theory, *J. Comput. Chem.*, 2020, **41**(21), 1931–1940.
37 K. Momma and F. Izumi, VESTA 3 for three-dimensional visualization of crystal, volumetric and morphology data, *J. Appl. Crystallogr.*, 2011, **44**(6), 1272–1276.
38 V. Wang, *et al.*, VASPKIT: A user-friendly interface facilitating high-throughput computing and analysis using VASP code, *Comput. Phys. Commun.*, 2021, **267**, 108033.
39 D. Bahamon, *et al.*, A DFT study of the adsorption energy and electronic interactions of the SO_2 molecule on a CoP hydrotreating catalyst, *RSC Adv.*, 2021, **11**(5), 2947–2957.